Hydrogen evolution at mixed α-Fe1 − xCrxOOH

Journal of Electroanalytical Chemistry 819 (2018) 114–122

Contents lists available at ScienceDirect

Journal of Electroanalytical Chemistry

journal homepage: www.elsevier.com/locate/jelechem

Hydrogen evolution at mixed α-$Fe_{1-x}Cr_xOOH$

Patrik Larses[a], Adriano S.O. Gomes[a,b], Elisabet Ahlberg[a], Michael Busch[c,*]

[a] Department of Chemistry and Molecular Biology, University of Gothenburg, Kemigården 4, SE-41296 Gothenburg, Sweden
[b] AkzoNobel Pulp and Performance Chemicals, SE-44580 Bohus, Sweden
[c] Department of Physics, Chalmers University of Technology, SE-41296 Gothenburg, Sweden

ARTICLE INFO

Keywords:
Hydrogen evolution reaction
Iron oxides
Chromium oxides
Electrocatalysis
Chlorate process

ABSTRACT

The activity of mixed α-$Fe_{1-x}Cr_xOOH$ oxides towards hydrogen evolution in alkaline solution is discussed based on Density Functional Theory (DFT) calculations, cyclic voltammetry and steady state measurements. Thermogravimetric and XRD measurements indicate an isomorphic substitution of Fe by Cr. Electrochemical characterization shows increasingly sluggish hydrogen evolution reaction (HER) kinetics with increased Cr loadings. This decrease in activity is accompanied by the inhibition of the reduction of iron in α-$Fe_{1-x}Cr_xOOH$. To investigate the origin of this decrease in activity, DFT calculations were performed for mixtures of Fe and Cr placed at $Fe(OH)_2$. Based on phase diagrams, the most stable structures under HER conditions are identified and used to estimate the theoretical overpotential. In contrast to experiment, no decrease in HER activity is observed. Instead, mixed FeCr sites display an overpotential comparable to that of Pt. Taking into account the inhibition of the bulk reduction in the presence of Cr, the activity decreases in agreement with experiment. These results are very important in the search for cathodes in the chlorate process that are active also in the absence of chromate in solution and may offer a new route for Pt free HER catalysts in alkaline solution.

1. Introduction

Reduction of water to H_2 is an industrially important reaction and serves as a reference reaction in electrocatalysis. This reaction is catalysed by Pt group metals at negligible overpotentials [1–6]. Mechanistically, the hydrogen evolution reaction (HER) starts with the discharge of a H^+ at the surface to form an adsorbed *−H species (Volmer reaction; * denotes an arbitrary adsorption site) [7–9]. This step is followed either by the recombination of 2 *−H moieties to H_2 (Tafel reaction) [8–10] or the direct formation of H_2 with a second H^+ (Heyrovsky reaction) [8,9,11]. In alkaline solution, water is the hydrogen source instead of protons. Recently, the development for hydrogen evolution on metals and alloys in alkaline solutions was reviewed [12]. The Volmer-Tafel-Heyrovsky reactions are also used to describe hydrogen evolution on non-metals such as metal-oxides [13,14], even though the active site for hydrogen adsorption differs compared to metals.

A central aim in current electrochemistry is the search for non-noble alternatives to Pt for the HER. Early, Gerischer [8] and Parsons [9] realized, that the activity of metallic HER catalysts can be ordered according to the binding energy of adsorbed H. Using the stability of H as a descriptor, the first volcano plots were constructed by Gerischer [8] and simultaneously by Parsons [9]. These volcanoes were later adapted and successfully used to identify promising electrocatalysts [6,15]. Recently, however, the applicability of volcano plots constructed from DFT has been challenged since only thermodynamics obtained from simplified model systems are considered. Indeed additional factors such as the position of the d-band in relation to the Fermi level and the interaction between the d-band and the hydrogen orbital, the double layer, conductivity of the substrate and the activation barriers associated with the discharge at the electrode are at least equally important [16,17]. Despite this, DFT calculations have had a large impact on the molecular understanding of electrocatalytic reactions [5,6,18].

While most of the considered HER electrocatalysts are based on metals or alloys [2,3], a large number of non-metallic materials have been discussed [12,19–22]. Indeed, metallic HER cathodes are not applicable in all cases as electrocatalysts. An industrially important example of this is the chlorate process, where the HER is the main cathodic reaction. In commercial chlorate plants, the cathode commonly consists of mild steel [23,24]. During plant shut-downs, the cathode corrodes and a range of different FeOOH species is formed [25]. Since undivided cells are used in the chlorate process, chromate needs to be added to the solution to inhibit side reactions such as hypochlorite and chlorate reduction [23,24]. Chromate is reduced at the cathode forming a hydrated chromium (III) film on the surface [24]. This leads to a complex surface composition where hydrogen evolution

* Corresponding author.
E-mail address: michael.busch@chalmers.se (M. Busch).

http://dx.doi.org/10.1016/j.jelechem.2017.09.032
Received 27 July 2017; Received in revised form 12 September 2017; Accepted 14 September 2017
Available online 22 September 2017

takes place under alkaline conditions [25]. In previous work [26], well defined corrosion products were synthesized and evaluated with respect to their hydrogen evolution kinetics under alkaline conditions, relevant for the technical application.

In what follows, we will discuss the influence of Cr on the activity of α-FeOOH towards the HER. In the first part we will discuss the synthesis and characterization of mixed α-$Fe_{1-x}Cr_xOOH$ and $Cr(OH)_3$ films, their stability and their performance towards hydrogen evolution. Our experiments indicate, that the HER activity of the electrode decreases with increased Cr content. The origin of the detrimental effect of Cr will be discussed based on DFT calculations.

2. Experimental and computational details

2.1. Synthesis of $Fe_{1-x}Cr_xOOH$

The synthesis of the Cr substituted α-FeOOH was based on earlier work of Schwertmann et al. [27]. 300 mL of 0.5 M $Cr(NO_3)_3{\cdot}9H_2O$ and 180 mL of 5.0 M KOH were added as different aliquots to 45 mL of 1.0 M $Fe(NO_3)_3{\cdot}9H_2O$ into separate polypropylene bottles. To each of these bottles, appropriate amounts of KOH were added and diluted to a final volume of 800 mL and 0.3 M in KOH. Samples were then agitated and maintained at 70 °C in an oven for 118 days. This is generally described as a hydrothermal synthesis, where a stepwise deprotonation of Fe(III) is induced by heating and addition of a base. During this phase, Fe(III) is isomorphically substituted by Cr(III) when that species is present [27].

2.2. Synthesis of the $Cr(OH)_3$

The $Cr(OH)_3$ nanoparticles were synthesized through a hydrothermal method proposed by Xu et al. [28]. 1 mmol acrylamide (Sigma-Aldrich, 99%) and 0.5 mmol of $K_2Cr_2O_7$ (Roth, 99%) were mixed in 38 mL of distilled water into an autoclave. The solution was stirred to get a homogeneous solution, sealed and heated up to 180 °C for 12 h. The $Cr(OH)_3$ nanoparticles were left to cool in room temperature and washed with 20–30 mL of distilled water and dried at 100 °C.

$Cr(OH)_3$ was also prepared as a thin film on a Fe rotating disc electrode. The $Cr(OH)_3$ electrodeposition was performed using the potentiostatic technique proposed by Aguilar et al. [29]. The electrodeposition bath formulation contain 364 g L^{-1} of CrO_3 (Sigma-Aldrich, 99,9%) and 9.1 g L^{-1} of $BaCO_3$ (Sigma-Aldrich, 99%). The iron rotating disk electrode (0.95 cm^2) was polished using SiC papers (Struers) and alumina polishing slurry (Struers), prior to electrodeposition. After polishing, the electrode was rinsed with distilled water, cleaned with ultra-sonication in distilled water and immediately immersed in the electrodeposition bath. The potential applied was − 1.6 vs Ag/AgCl, and the deposition time was 30 min. Later, the iron electrode covered with $Cr(OH)_3$ was vigorously rinsed with distilled water, dried and stored in air at room temperature. The electrode potential was controlled by an AutoLab PGSTAT72461 during the electrodeposition experiments.

2.3. Thermal analysis

Thermogravimetry (TG) and Differential scanning calorimetry (DSC) were conducted with a NETZSCH STA 409 PC/PG instrument with a flow of air (80% N_2 and 20% O_2) over a range of 20–800 °C with a heating rate of 10 °C min^{-1}. An alumina crucible was used for the analysis of samples (between 20 and 40 mg) that had been stored in a desiccator before use.

2.4. Powder X-ray diffraction (XRD)

The diffractograms were collected with a Bruker AXS D8 Advance (Cu Kα = 1.5418 radiation) equipped with a LynxEye detector set to lock coupled scan in the range of 16–65 2θ and with a step size of 0.025 and 1.5 s $step^{-1}$. Silicon standard powder (Nist 640C) was added in a ratio of 1:9 to the samples before analysis. Recorded diffractograms were indexed based on the first peak for the silicon powder at 28.4409 corresponding to *hkl* of 111.

2.5. Preparation of electrodes

Electrodes were prepared by mixing the synthesized powders with carbon paste (Surfactrode Refill paste (6.2319.000), Metrohm). The ratio $Fe_{1-x}Cr_xOOH$:C mixture was kept at 1:9. Electrodes were prepared by filling the RDE with carbon paste and packed with a piston. A 0.6 mm deep cavity was extracted and removed from the carbon paste and the void was filled with the $Fe_{1-x}Cr_xOOH$:C mixture. The surfaces were pressed and cut with a glass slide. Surface smoothness and packing were evaluated with a Nikon SMZ800 optical microscope coupled with an Axiocam 105 colour camera. All surfaces were rinsed with Milli-Q water and gently wiped with a tissue before use. The geometric surface area for the electrodes was determined with the help of a commercial software (Zen 2012, blue edition provided by Carl Zeiss Microscopy GmbH) to 0.12 cm^2.

2.6. Electrochemical cell

All materials were placed, one at a time, as working electrodes in a three electrode cell. A Princeton Parstat 4000 + and a Gamry600 potentiostat were used for the electrochemical measurements. A platinum half-open cage was used as counter-electrode. The reference electrode, Ag/AgCl (3 M KCl, + 0.210 V vs. nhe) was placed inside a double junction with a pore diameter of 1 mm and filled with electrolyte. The glass vessel was filled with 70 mL of 0.2 M sodium sulfate, Na_2SO_4 (Scharlau, 99,5%), adjusted to pH 11 as electrolyte. Prior to all electrochemical measurements, the electrolyte was purged with nitrogen gas for a minimum of 30 min, with the working electrode rotating at a speed of 2500 rpm, while the open circuit potential was monitored. Unless otherwise stated, all usage of water refers to ultrapure Milli-Q water (18.2 MΩ at 25 °C) and chemicals with purity ≥ 99% from Sigma-Aldrich.

2.7. Electrochemical measurements

The HER was evaluated by means of Cyclic Voltammetry (CV) and steady state measurements. Experiments started with an impedance measurement at open circuit potential with a frequency range of 100 kHz–10 mHz, directly followed by cyclic voltammetry in the potential range of 0.0 to − 1.7 V vs Ag/AgCl with a sweep rate of 5 mV s^{-1}. A RDE filled with only carbon paste was analysed with the same procedures to establish the background. All cyclic sweeps have been corrected for the uncompensated solution resistance. After the voltammetry, the current was monitored at constant potential with concomitant impedance measurements, in the potential range from − 1.7 to − 0.8 V vs Ag/AgCl and with a potential step of 0.1 V.

2.8. Computational details

All calculations were performed with VASP (version 5.4.1). Transition metal compounds are known to suffer from static correlation [30–32]. Following the recommendation of Grimme [33] and based on the comparison of high-level ab-initio calculations with DFT, suggesting a better performance of semi-local functionals [31], we relied on the Generalized-Gradient Approximation (GGA) PBE-dDsC [34–37] functional, which includes density dependent van der Waals corrections. 3 × 1 × 1 (4 × 1 surfaces), 9 × 9 × 9 ($Fe(OH)_2$ bulk), 9 × 9 × 1 (Fe (111) and 15 × 15 × 15 (Fe bulk) k-point sets in combination with a plane-wave cut-off of 550 eV were used. For molecules, the k-point set was reduced to the Γ-point. The core electrons were approximated by

Projector Augmented Wavefunctions (PAW) [38]. To aid the convergence of the wave function, a smearing of 0.1 eV was added. Electronic convergence was assumed for energy changes below 10^{-6} eV and structural convergence for forces below 0.05 eV $Å^{-1}$. Spin was treated explicitly for the oxides by assuming a high spin electronic configuration and ferromagnetic coupling between the transition metal ions. This procedure has been successfully applied to a large number of comparable transition metal oxides [39–44]. At metallic Fe systems, the spin was allowed to vary freely. Conversion from electronic energies to Gibbs Free energies was achieved by adding constant corrections for zero-point energy and entropy contributions [45,46]. Redox potentials are computed using the theoretical normal hydrogen electrode (nhe) [46]. If not stated otherwise, all computational redox potentials are given versus the nhe.

According to experimental findings [26,47], goethite is reduced prior to hydrogen evolution. In-situ Raman measurements indicate, that $Fe(OH)_2$ is formed in the reduction process [47]. Accordingly, a bulk + II state was assumed to be present under HER conditions. Thus, the HER activity of FeCr hydroxides were computed using a layered Fe $(OH)_2$ model system which displays a brucite type structure [48]. Following previous studies on comparable layered catalysts, only edge sites were considered as potential active sites [19,21,49]. The electrochemical properties were computed using a 4 × 4 × 1 unit cell with 2 monolayers fixed into bulk positions. The backside of the slab was terminated such, that all Fe ions display the correct + II oxidation state of the bulk. To avoid interactions between the slabs, a vacuum of at least 15 Å was added in the (010) direction, while the DFT bulk lattice parameters were used in (001) and (100) direction. The influence of Cr addition was studied by replacing surface Fe ions by Cr. The relevant surface configurations under reaction conditions were obtained from phase diagrams computed following the procedure described by Su et al. [50]. To reduce the complexity of the structural optimizations, weakly bound water adsorbates were replaced by bare adsorption sites for the purpose of computing phase diagrams. Once the most stable surfaces were identified, explicit water molecules were added at the unoccupied adsorption sites for the purpose of computing the HER reaction energies.

3. Results and discussion

3.1. Characterization

Five α-FeOOH samples with different degrees of Cr isomorphically substituted in the structure were synthesized. The dried materials were presented as powders, with brown-reddish colour, typical for FeOOH. The amount of Cr incorporated in the structure was analysed with XRF. The theoretical (based on Cr amount in solution, and considering 100% reaction yield) and experimentally measured Cr contents are present in Table 1. XRF analyses (Table 1) show that not all chromium has been substituted into the structure, which is in agreement with earlier findings [27].

XRD studies of the synthesized materials were used to elucidate the crystallinity and evaluate the influence of Cr in the α-FeOOH structure. In Fig. 1, the diffractograms for α-FeOOH and α-$Fe_{1-x}Cr_xOOH$ are summarized. All samples show good crystallinity with sharp and well defined peaks. Narrow peaks at 28.4°, 47.2° and 56.0°, marked with

Table 1
Theoretic and measured at.%Cr substituted into α-FeOOH using XRF.

Sample	Theoretical at% Cr	Measured at% Cr
1	0.0	0.0
2	0.68	0.54
3	1.47	1.15
4	2.07	1.61
5	3.32	2.75

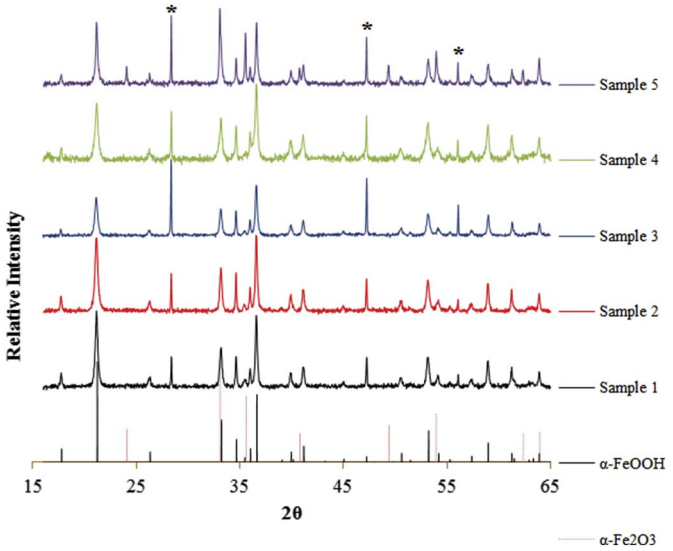

Fig. 1. Diffraction patterns for Cr substituted α-FeOOH samples. Sample 1 = α-FeOOH, Sample 2 = 0.54% Cr, Sample 3 = 1.15 at% Cr, Sample 4 = 1.61 at% Cr, Sample 5 = 2.75 at% Cr. Reference diffractograms α-FeOOH (PDF card 04-015-2898) and Fe_2O_3 (PDF card 01-073-8431). Peaks marked with a star originates from Si used as an internal standard.

stars, correspond to silica powder added as an internal standard. The reference XRD reflections of α-FeOOH (PDF 04-015-2898) and α-Fe_2O_3 (PDF 01-073-8431) are also shown (red-dotted and blue-dotted lines, respectively). All samples show characteristic peaks for α-FeOOH only, except for the sample containing 2.75 at% Cr, which also shows extra peaks at 24.1, 35.5, 49.3 and 62.3°, corresponding to α-Fe_2O_3. Schwertmann et al. [27] show a decrease in cell parameters and less crystalline products as the Cr substitution increases. In the limited substitution range used in the present paper, these differences could not be detected. Despite the appearance of hematite (α-Fe_2O_3) in the sample with the highest amount of Cr incorporated (2.75 at%), the sample still mainly represents the properties of Cr substituted goethite.

Since XRD is not conclusive regarding substitution of Cr(III) in the goethite structure, other techniques such as Raman spectroscopy [51], FT-IR [52,53], X-ray scattering [54], EXAFS [55], XANES and thermogravimetry [56] have been used. In the present paper, we relied, inspired by the work of Tang et al. [56], on thermal analysis. They have shown for ferrihydrite as the end product of the pure iron phase, that a "solid solution" with chromium appears differently compared to mixed powders of ferrihydrite and the pure precipitated chromium hydroxide.

In Fig. 2, the TG analysis of samples 1–5 (solid lines) are compared to those obtained for pure $Cr(OH)_3$ and a mixture of $Cr(OH)_3$/α-FeOOH (50/50% mortared together). The weight losses for α-$Fe_{1-x}Cr_xOOH$ occur in two stages, where the first stage is interpreted as loss of structural water, and ranges between 70 and 250 °C for α-FeOOH and Samples 2 and 3, 70–275 °C for Sample 4 and 70–325 °C for Sample 5 (Fig. 2a). This effect is concomitant with broad endothermic peaks shown in the DSC data, Fig. 2b, which is typical for water evaporation. There is a gradual increase in mass loss in this region with increasing Cr substitution, which indicates, that Cr attracts more loosely bound water. For the two highest substitution levels three different stages for mass loss can be observed, similar to the results for $Cr(OH)_3$ [56].

Immediately after the first stage of mass loss a sharp decrease in weight is observed (Fig. 2a), indicating a second stage of water evaporation. At the same time, a second endothermic peak appears in the DSC curve (Fig. 2b), due to conversion of α-FeOOH to α-Fe_2O_3. The temperature where the second mass loss starts and the position of the endothermic peak in the DSC increases with increasing Cr in the structure. It is well known that Cr stabilizes the goethite structure [27,57], making the total dehydration of α-FeOOH and conversion to α-

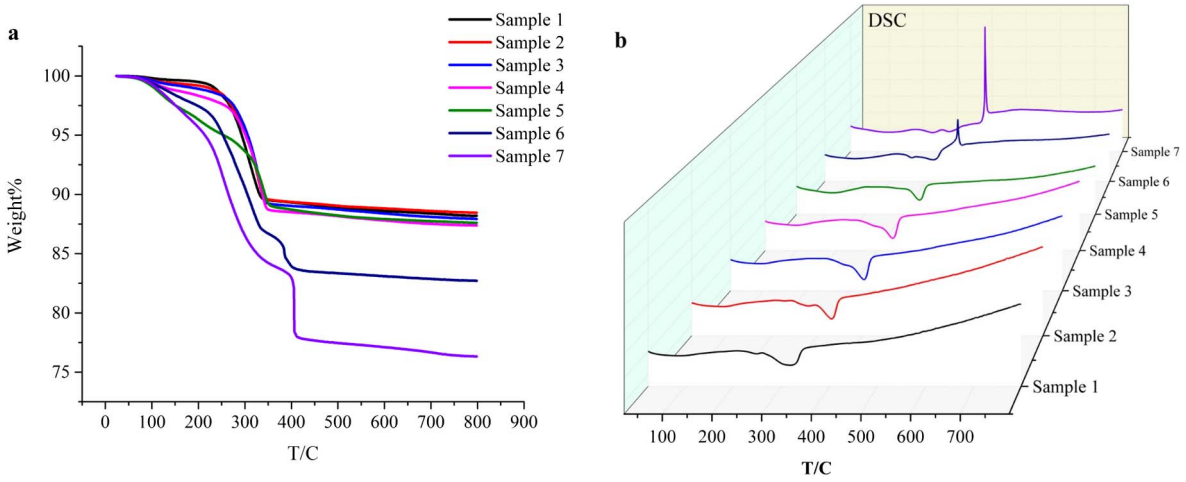

Fig. 2. Thermogravimetric (a) and differential calorimetric (b) analysis of Cr substituted α-FeOOH. Sample 1 = α-FeOOH, Sample 2 = 0.54% Cr, Sample 3 = 1.15 at% Cr, Sample 4 = 1.61 at% Cr, Sample 5 = 2.75 at% Cr, Sample 6 = 50% α-FeOOH + 50% $Cr(OH)_3$, Sample 7 = $Cr(OH)_3$.

Fe_2O_3 more difficult. It is important to notice that the presence of Cr does not affect the total amount of water loss, providing proof, that the substitution is indeed isomorphic. The mass loss corresponds to approximately 1.5 water molecule per α-$Fe_{1-x}Cr_xOOH$ unit.

The TG analyses for the synthesized materials show clear differences compared with TG data for $Cr(OH)_3$ and the $Cr(OH)_3$/α-FeOOH mixture. The TG curve for $Cr(OH)_3$ shows that dehydration of this material occurs in three main steps [56]: evaporation of surface-adsorbed water, dehydration of structural water and condensation of water from CrOOH forming Cr_2O_3. The first two steps are concomitant with endothermic peaks (Fig. 2b) and, the third, with a sharp exothermic peak. This result is in agreement with Gomes et al. [58], focusing on $Cr(OH)_3$. The mixture $Cr(OH)_3$/α-FeOOH shows an intermediate TG curve between pure $Cr(OH)_3$ and pure α-FeOOH, as expected for a mixture of two compounds. From these TG and DSC results it can be concluded that chromium is incorporated in the goethite structure.

3.2. Electrochemical characterization

To evaluate the electrochemical properties of the Cr substituted α-FeOOH, samples 1–5 were mixed with a conducting carbon paste and pressed into an RDE. The analyses were done by means of cyclic voltammetry (CV) sweeps and steady-state polarization (SS) obtained during impedance measurements.

The cyclic voltammetry is shown in Fig. 3, where the sweeps in negative and positive going directions are separated for clarity. In the negative going direction (Fig. 3a), the reduction of α-FeOOH (black line) starts at approximately − 1.0 V and the current levels off prior to the hydrogen evolution reaction. On the positive going scan (Fig. 3b), the corresponding oxidation is observed as a broad peak at − 0.3 V. The redox properties of α-FeOOH are well established and the reduction leads to an "$Fe(OH)_2$" type structure which is oxidized reforming α-FeOOH or other oxy-hydroxide compounds depending on the conditions [25,26,47,59–63]. The reduction process is very slow, indicating a rate limiting transport in the solid phase, i.e. a fast surface reduction is followed by a slow reduction of the bulk material [47].

In the presence of chromium in the goethite structure, the reduction current decreases and is practically absent for the mixed compound with 2.75 at% Cr (Fig. 3a). A corresponding decrease in the oxidation current is observed in the positive going sweep (Fig. 3b). It appears, that substituting with chromium stabilizes the Fe(III) state. A stabilization of Cr-goethite compared with native goethite has been reported in the context of dissolution studies [27,57]. The overpotential for the HER is higher than for pure α-FeOOH but no specific trend could be observed. This is not surprising, since it has been shown, that the HER on α-FeOOH can only take place on the reduced surface [26]. For comparison, additionally also pure $Cr(OH)_3$ on iron was investigated and the results are shown for the negative going scan together with

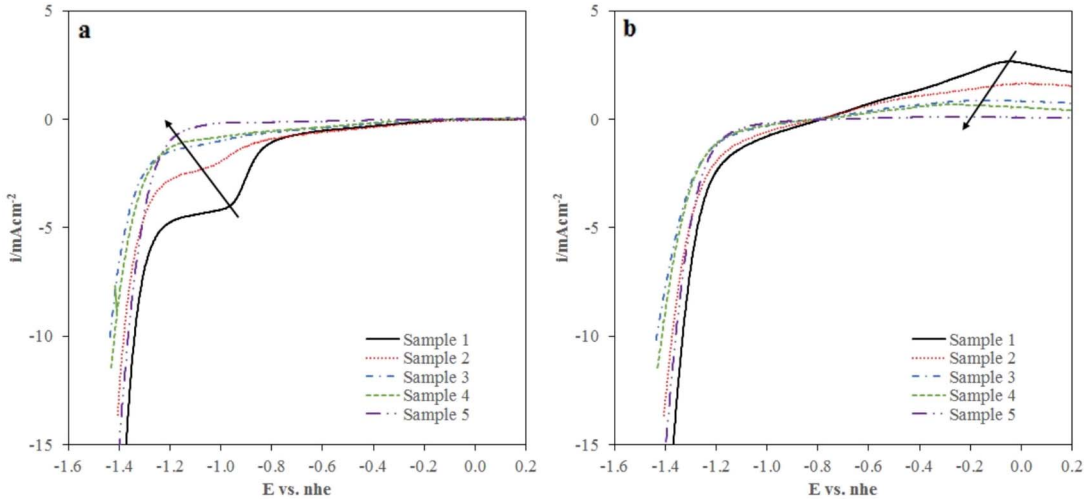

Fig. 3. a) Sweeps in the negative going direction and b) Sweeps in the positive going direction. Sample 1 = α-FeOOH, Sample 2 = 0.54% Cr, Sample 3 = 1.15 at% Cr, Sample 4 = 1.61 at% Cr, Sample 5 = 2.75 at% Cr. Sweep rate 5 mV s^{-1}. Fe/$Cr(OH)_3$ is deposited $Cr(OH)_3$ on Fe substrate. Sweep rate 2 mV s^{-1}. Electrolyte 0.2 M Na_2SO_4, pH = 11.

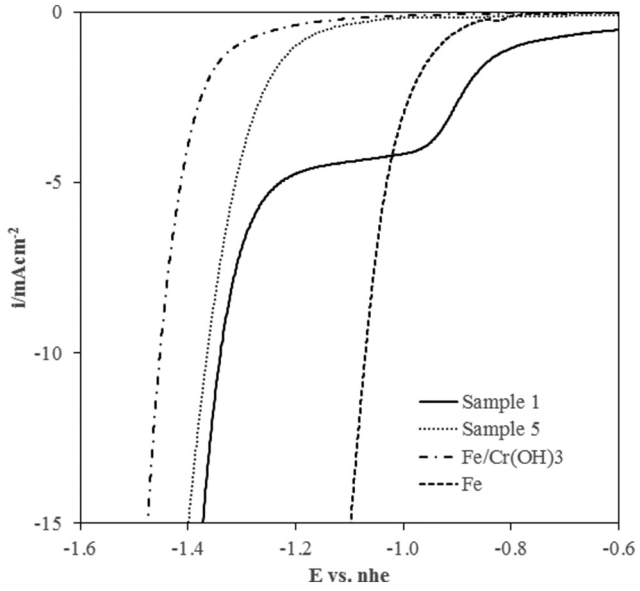

Fig. 4. Sweeps in the negative going direction Sample 1 = α-FeOOH, Sample 5 = 2.75 at % Cr (sweep rate 5 mV s^{-1}), $Fe/Cr(OH)_3$ is deposited Cr(OH)3 on Fe substrate (sweep rate 2 mV s^{-1}). Electrolyte 0.2 M Na_2SO_4, pH = 11.

results on polished iron, α-FeOOH and α-FeOOH with 2.75% Cr (Sample 5) (Fig. 4). The overpotential for the HER increases in the order:

$$Fe < \alpha - FeOOH < \alpha - FeOOH \text{ with } 2.75\%Cr < Cr(OH)_3 \text{ on } Fe$$

Previous experiments on two different iron oxy-hydroxides, α-FeOOH and γ-FeOOH have shown, that the overpotential for hydrogen evolution decreases with almost 300 mV after reduction of the surface. These experiments also showed, that the active site for hydrogen evolution is independent of the starting material and as active as polished mild steel [26]. Steady state measurements were made also for the mixed compound and the activity for hydrogen evolution increases compared with the results from the cyclic voltammetry (Fig. 5). A clear trend is observed with increasing overpotential as the chromium content increases. This is in line with the difficulty in reducing the mixed

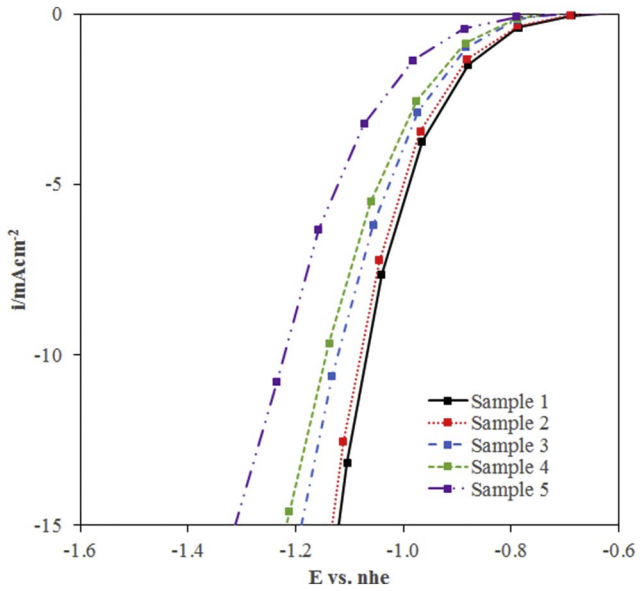

Fig. 5. Steady state currents obtained during impedance measurements. Sample 1 = α-FeOOH, Sample 2 = 0.54% Cr, Sample 3 = 1.15 at% Cr, Sample 4 = 1.61 at% Cr, Sample 5 = 2.75 at% Cr. Sweep rate 5 mV s^{-1}. Electrolyte 0.2 M Na_2SO_4, pH = 11.

materials. Interestingly, the activity is not as high as for polished iron. However, the results on the mixed compounds indicate that the activation process is very slow and true steady state currents are probably not recorded. The slow reduction of the material supports a solid state mechanism, which is limited by transport of water or hydroxide ions in the structure. The very slow rate of ligand exchange for Cr(III) might contribute to the slow process.

3.3. Determining the surface configuration

DFT calculations were used to rationalize the influence of Cr in α-FeOOH on the thermodynamics of the HER. In accordance with the reduction of bulk Fe(III) to Fe(II) at negative potentials shown in Fig. 3 and reported in the literature [26,47], a $Fe(OH)_2$ model system with a brucite type structure was used. The starting point for studying the influence of Cr substitution on the activity of Fe oxides is the determination of the active phase under conditions relevant for the chlorate process. Assuming a pH of 11, in total 6 FeCr surface terminations with 0%, 25%, 50%, 75% and 100% Cr at the edge are considered. To reduce the complexity, incorporation of Cr into the structure is neglected. Independent of the detailed FeCr composition at the edge, in total 4 cus and 4 bridged adsorption sites are available and can be occupied by either *−OH_2, *−OH or *=O groups. Following previous work [44,45], we assume a bare site rather than explicitly adsorbed water molecules to avoid complications from weakly bound adsorbates.

Without addition of Cr, a pure Fe terminated edge is at hand (Fig. 6a). Under these conditions a very low coverage of only 2 *−OH groups adsorbed to bridged sites is observed. This formally corresponds to the formation of Fe(I)/Fe(II) sites at the edge. However, this structure is inherently unstable and immediately reconstructs by shifting threefold *−OH groups into bridged positions at the edge. Simultaneously, the Fe-Fe distance decreases to only 2.44 Å, which is typical for metallic Fe [64]. Thus, the formation of larger Fe nanoparticles in an experimental environment can under these conditions not be excluded, as it is inhibited by the restrictions imposed by the model system. Identical reconstructions were also observed when adding 25% or 50% Cr to the edge but inhibited at higher Cr loadings. Conversion to even lower coverages was observed at significantly more negative potentials of approximately − 1.3 V vs. nhe. At the same time, a transition to a high coverage structure, with 6 *−OH distributed into 4 bridged and 2 cus sites, becomes favourable at potentials more positive than − 0.8 V vs. nhe. This coincides with the experimentally observed onset of water reduction. Based on these results, a low coverage structure with 2 *−OH groups at the surface, or even the formation of Fe nanoparticles during the HER, could be expected. However, this transition has, to the best of our knowledge, so far not been observed. Keeping this in mind, we considered both metallic Fe and the possibility of a 6 *−OH terminated surface as possible HER catalysts.

Moving to a Cr coverage of 25%, higher *−OH coverages become more favourable (Fig. 6b). At very negative potentials, structures with 1 *−OH or 2 *−OH groups are still favoured. Similar to the Fe terminated edge, a reconstruction to Fe_3 nanoparticles is observed for these structures. At potentials more positive than − 1.1 V vs. nhe a high coverage structure with 5 *−OH groups is most stable. Considering the experimental onset of − 0.8 V vs. nhe, this structure must be expected under HER conditions.

Adding 50% Cr, the Cr may either be distributed in an alternating or adjacent fashion (Fig. 6c and d). The exact Cr distribution has significant influence on the surface configuration. Assuming an alternating fashion, a coverage of 4 *−OH groups is stable at potentials below − 1.1 V vs. nhe. At more positive potentials a conversion to a slightly higher coverage with 5 *−OH groups is observed (Fig. 6d). Accordingly, mainly 5 OH groups are present under HER conditions. For Cr ions placed adjacent to each other, generally higher coverages are preferred (Fig. 6c). The 4 *−OH coverage is converted directly to a 6 *−OH

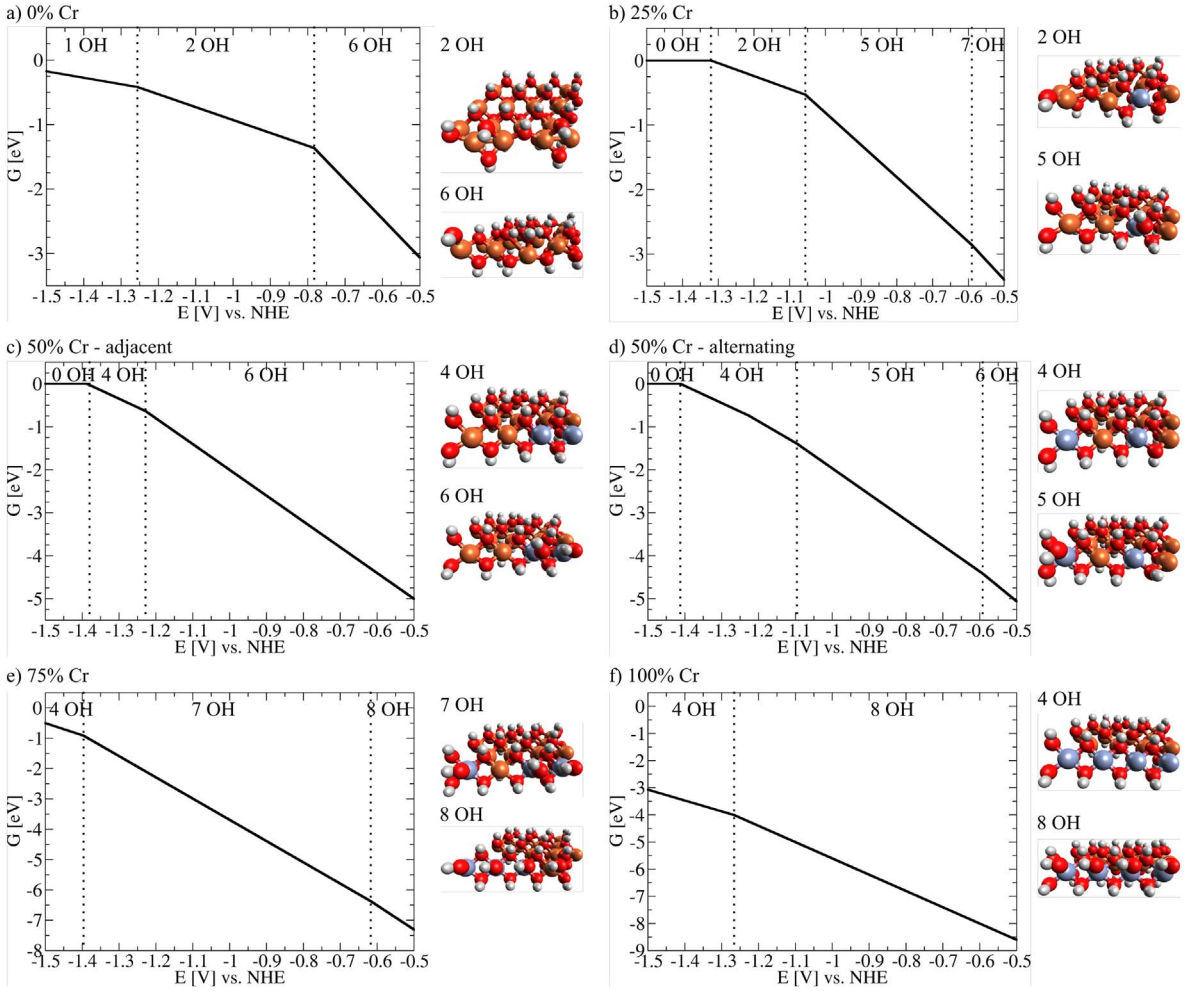

Fig. 6. Calculated surface stabilities at pH 11 and the corresponding surface terminations are depicted. Colorcode: Orange: Fe; grey: Cr; red: O; white: H.

coverage already at a potential of only − 1.2 V vs. nhe, rendering this structure the most likely candidate for the HER.

The trend towards higher OH coverages is continued for 75% and 100% Cr at the edge (Fig. 6e and f). In case of the former a surface with 7 *−OH is the sole stable structure within a potential range between − 1.4 V and − 0.6 V vs. nhe (Fig. 6e). A fully OH covered surface with 8 *−OH groups is finally observed at potentials more positive than − 1.3 V vs. nhe for a fully Cr covered edge (Fig. 6f). Accordingly these structures are considered as active phases during HER.

3.4. Assessing the activity of Cr doped goethite

Based on our analysis of the most stable phases, it becomes possible to estimate the activity of the different FeCr surface terminations towards H_2 evolution. The theoretical overpotential will be estimated based on a purely thermodynamic assessment of the H binding energy to the active site. In the context of surface complexation at oxide surfaces, the active site comprises either a transition metal TM−OH or TM═O species. Depending on the nature of the transition metal and the pH of the solution, the degree of protonation varies. Using the 2pK model [65], the active site can be written as $TM-OH^0$ for α-FeOOH. Adding a proton gives $TM-OH_2^+$ and the subsequent reduction will result in an adsorbed hydrogen, $TM-OH-H_{ads}$ [26]. A comparable mechanism is expected when proceeding through a TM═O precursor, i.e. a protonation to $TM-OH^+$ is followed by a discharge resulting in an adsorbed hydrogen $TM-O-H_{ads}$. To emphasize this difference we will denote the adsorption site with # rather than the *, commonly used in literature. # corresponds, depending on the precursor, either to a TM−OH or TM = O moiety placed in cus or bridged position. Considering a thermodynamics only picture and neglecting all charged intermediates, the HER is reduced to:

$$\# + H^+ + e^- \rightarrow \# - H \quad (1)$$

$$\# - H + H^+ + e^- \rightarrow H_2 + \# \quad (2)$$

As a best case scenario, this assessment allows a quick comparison of different catalysts and to rule out poorly performing materials.

In Fig. 7, activities of the most active sites for the different FeCr edge configurations are summarized. Assuming a Fe terminated edge, several situations must be considered. Based on our computational

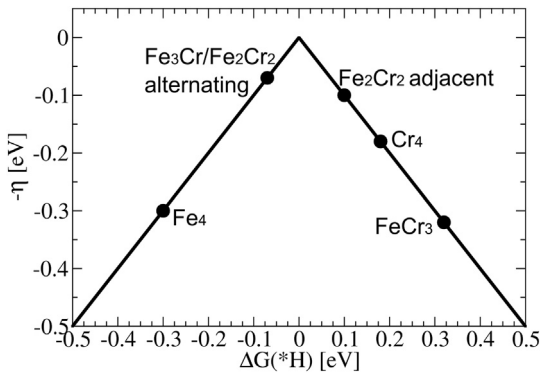

Fig. 7. The activity of the most active sites at different FeCr terminated $Fe(OH)_2$ is depicted.

phase diagram either a low coverage situation with only 2 *−OH groups in bridged positions or a high coverage situation with 6 *−OH moieties can be expected. Having observed the formation of Fe nanoparticles in our low coverage model system, we decided to study the activity of oxidized Fe(111). H_2 evolution proceeding through an oxidized Fe(111) surface was considered explicitly while values for H directly adsorbed at Fe(111) were taken from literature [3]. Our calculations indicate a *=O moiety placed in a threefold position as the most active site displaying an overpotential of only 0.1 eV. This is significantly lower than the overpotential previously reported for H adsorbed to Fe(111) [3]. Moving to a high coverage termination with 6 *−OH groups at the edge, the HER proceeds through a Fe−OH_2 intermediate and the overpotential increases to 0.3 eV. According to our calculations, freshly polished Fe electrodes should display a significantly higher activity. This is indeed also observed experimentally (see Fig. 4). Under steady-state conditions, however, the experimental overpotential for $Fe_{1-x}Cr_xOOH$ decreases, and for pure goethite the activity becomes independent of the history of the electrode. This clearly rules out the possibility of metallic nanoparticles acting as active sites at Fe oxide covered electrodes. Instead, the 6 *−OH covered surface appears to be more realistic.

Adding minor amounts of Cr to the edge has a strong beneficial effect on the HER properties of $Fe(OH)_2$ with 25% Cr mixed into the edge, the overpotential drops to only 0.1 eV. Indeed the activity of these sites is comparable to the HER at Pt [66]. Under these conditions, the HER proceeds at a Fe−OH_2 cus site activated by an adjacent Cr ion. Fe sites not directly adjacent to Cr display an overpotential comparable to that of a Fe covered edge. Moving to even higher Cr coverages of 50%, the activity of the mixed FeCr edge remains high. Independent of whether the Cr ions are placed in an alternating fashion or are placed directly adjacent, a very low overpotential of only 0.1 eV is observed. For Cr ions placed adjacent to each other, an Fe−OH group next to the Cr ions acts as active site. This emphasizes again the beneficial role of traces of Cr at the surface. For Cr ions placed in an alternating fashion, each Fe is surrounded by 2 edge Cr ions. This slightly increases the overpotential at the Fe−OH_2 active site and the Fe-(OH)-Cr group becomes the most active site.

Above 50% Cr at the edge, the activity towards HER starts to decrease again. For an edge with 75% Cr, the overpotential increases to 0.3 eV with cus Cr−OH or groups acting as HER centres, through a Cr−OH_2 intermediate. The previously most reactive Fe−OH_2 groups display, with an overpotential of 0.4 eV, a comparable activity. Interestingly, the overpotential drops slightly to only 0.2 eV for a fully Cr terminated edge. Here cus Cr−OH act as reaction centres.

According to our DFT results, Fe and Cr terminated surfaces should display equivalent activity for the HER. In fact, the activity should even increase due to the formation of beneficial mixed FeCr sites, upon addition of minor amounts of Cr. This is, however, not observed experimentally. Instead, the overpotential increases steadily with increasing amounts of Cr in the structure, and reaches a maximum for pure Cr $(OH)_3$. The discrepancy between calculations and experiments can have several explanations. One reason could be shortcomings in the model systems used as a basis for DFT modelling. The experiments were performed on goethite that reduces to $Fe(OH)_2$ during hydrogen evolution. As discussed in Section 3.2, the reduction of the bulk phase is slow, but it is reasonable to assume, that a bulk Fe(II) structure is the best model for computational studies. In addition, goethite and $Fe(OH)_2$ have similar layered structures and display comparable surface sites [67]. Also, comparing the activity of Mn oxides towards water oxidation in very different embeddings showed, that the catalytic properties of oxides are relatively robust with respect to very different embeddings [41,42,44,68,69].

The voltammetry of α-FeOOH with different Cr contents (see Fig. 3) clearly shows a decrease of the peak at − 0.9 V nhe, which is associated with the reduction of α-FeOOH to $Fe(OH)_2$. This reduction is limited by transport in the solid phase and inhibited at higher Cr loadings. All calculations were, however, performed assuming a Fe(II) bulk. To explore the effect of an inhibition of the bulk reduction, additional calculations assuming a Fe(III) bulk were performed. For the sake of simplicity only a Fe_4 termination with 6 OH groups is considered. Under these conditions, the HER overpotential increases by 0.5 eV to 0.8 eV for a non-reduced bulk. Accordingly, a reduced bulk is, in agreement with the experiments, required for the HER to proceed at relatively low overpotentials.

An additional limitation of DFT modelling of electrocatalysts is the difficulty to explicitly consider conductivity of the electrocatalysts since it is highly dependent on the presence of already minor amounts of defects or impurities [17]. Goethite is a n-type semiconductor, while chromium oxide has p-type conduction [70]. Mixtures of isostructural iron and chromium oxides gives a complex semiconducting behaviour [71]. Accordingly an electron transfer from the electrode to the proton can be achieved comparably easy for α-FeOOH but adding Cr to the structure may influence the conduction and lower the rate of reduction reactions [72]. This converts into an additional contribution to the overpotential and could explain the increased overpotential observed in experiment.

4. Conclusions

In summary α-$Fe_{1-x}Cr_xOOH$ samples with varying percentages of Cr isomorphically substituted into goethite were synthesized and characterized by XRD and TG. CV and steady state measurements indicate a decrease of the activity towards HER with increasing Cr content. The lowest activity was finally observed for pure $Cr(OH)_3$. The decrease in activity is accompanied by the inhibition of the reduction of α-FeOOH to $Fe(OH)_2$ with increasing Cr content. The electrochemical behaviour was rationalized by DFT calculations. In the first step, suitable surface diagrams were constructed and the most stable surface configurations extracted. Our calculations show a clear trend towards higher OH coverages with increased Cr content at the edge. Estimating the HER activity of the different surfaces by DFT indicates, in contrast to experiment, a comparable activity of edges terminated by Fe or Cr. The theoretical overpotential even drops to values comparable to Pt for mixed FeCr terminated edges. A significant increase of the overpotential is, however observed when taking into account the blocking of bulk reduction from α-FeOOH to $Fe(OH)_2$. Additionally, the electron conduction is blocked in Cr oxides by the p-type semiconducting behaviour [70].

The combined experimental and theoretical study clearly demonstrates that the activity of iron and chromium hydroxides towards HER is not limited by different active sites on the surface but rather by the bulk conduction and the inhibition of the reduction of bulk α-FeOOH to $Fe(OH)_2$. These results are very important in the search for cathodes in the chlorate process that are active also in the absence of chromate in solution.

Acknowledgements

Financial support from the Swedish Research Council (grant no. 621-2010-4035) and AkzoNobel Pulp and Performance Chemicals AB is gratefully acknowledged.

Appendix A. Supplementary data

Supplementary data to this article can be found online at https://doi.org/10.1016/j.jelechem.2017.09.032.

References

[1] S. Trasatti, Work function, electronegativity, and electrochemical behaviour of metals: III. Electrolytic hydrogen evolution in acid solutions, J. Electroanal. Chem. 39 (1972) 163–184.

[2] J. Greeley, T.F. Jaramillo, J. Bonde, I. Chorkendorff, J.K. Nørskov, Computational high-throughput screening of electrocatalytic materials for hydrogen evolution, Nat. Mater. 5 (2006) 909–913.
[3] J. Greeley, J.K. Nørskov, Large-scale, density functional theory-based screening of alloys for hydrogen evolution, Surf. Sci. 601 (2007) 1590–1598.
[4] E. Skulason, V. Tripkovic, M.E. Björketun, S. Gudmundsdottir, G. Karlberg, J. Rossmeisl, T. Bligaard, H. Jonsson, J.K. Nørskov, Modeling the Electrochemical Hydrogen Oxidation and Evolution Reactions on the Basis of Density Functional Theory Calculations, J. Phys. Chem. C 114 (2010) 18182–18197.
[5] J.K. Nørskov, T. Bligaard, A. Logadottir, J.R. Kitchin, J.G. Chen, S. Pandelov, U. Stimming, Response to "Comment on 'Trends in the Exchange Current for Hydrogen Evolution' [J. Electrochem. Soc., 152, J23 (2005)]" miscellaneous, J. Electrochem. Soc. 153 (2006) L33.
[6] J. Greeley, N.M. Markovic, The road from animal electricity to green energy: combining experiment and theory in electrocatalysis, Energy Environ. Sci. 5 (2012) 9246–9256.
[7] T. Erdey-Gruz, M. Volmer, Z. Phys. Chem. Abt. A 150 (1930) 203.
[8] H. Gerischer, Mechanismus der Elektrolytischen Wasserstoffabscheidung und Adsorptionsenergie von Atomarem Wasserstoff, Bull. Soc. Chim. Belg. 67 (1958) 506–527.
[9] R. Parsons, The rate of electrolytic hydrogen evolution and the heat of adsorption of hydrogen, Trans. Faraday Soc. 54 (1958) 1053–1063.
[10] J. Tafel, Z. Phys. Chem. Abt. A 50 (1905) 641.
[11] J. Heyrovsky, Recl. Trav. Chim. Pays-Bas 44 (1925) 499.
[12] F. Safizadeh, E. Ghali, G. Houlachi, Electrocatalysis developments for hydrogen evolution reaction in alkaline solutions – a review, Int. J. Hydrog. Energy 40 (2015) 256–274.
[13] S. Trasatti, J. Lipkowski, P.N. Ross (Eds.), Electrochemistry of Novel Materials, VCH, New York, 1994.
[14] S. Trasatti, A. Wieckowsky (Ed.), Interfacial Electrochemistry: Theory, Experiment, and Applications, Marcel Dekker Inc, Basel, 1999.
[15] J.K. Nørskov, T. Bligaard, A. Logadottir, J.R. Kitchin, J.G. Chen, S. Pandelov, U. Stimming, Trends in the exchange current for hydrogen evolution, J. Electrochem. Soc. 152 (2005) J23–26, http://dx.doi.org/10.1149/1.1856988.
[16] W. Schmickler, S. Trasatti, Comment on "Trends in the Exchange Current for Hydrogen Evolution" [J. Electrochem. Soc., 152, J23 (2005)], J. Electrochem. Soc. 153 (2006) L31–L32.
[17] P. Quaino, F. Juarez, E. Santos, W. Schmickler, Volcano plots in hydrogen electrocatalysis—uses and abuses, Beilstein J. Nanotechnol. 5 (2014) 846–854.
[18] J.K. Nørskov, T. Bligaard, J. Rossmeisl, C.H. Christensen, Towards the computational design of solid catalysts, Nat. Chem. 1 (2009) 37–46.
[19] T.F. Jaramillo, K.P. Jørgensen, J. Bonde, J.H. Nielsen, S. Horch, I. Chorkendorff, Identification of active edge sites for electrochemical H_2 evolution from MoS_2 nanocatalysts, Science 317 (2007) 100–102.
[20] J. Kibsgaard, T. Jaramillo, Molybdenum phosphosulfide: an active, acid-stable, earth-abundant catalyst for the hydrogen evolution reaction, Angew. Chem. Int. Ed. 53 (2015) 14433–14437.
[21] B. Hinnemann, P.G. Moses, J. Bonde, K.P. Jørgensen, J.H. Nielsen, S. Horch, I. Chorkendorff, J.K. Nørskov, Biomimetic hydrogen evolution: MoS_2 nanoparticles as catalyst for hydrogen evolution, J. Am. Chem. Soc. 127 (2005) 5308–5309.
[22] M.H. Hansen, L.-A. Stern, L. Feng, J. Rossmeisl, X. Hu, Widely available active sites on Ni_2P for electrochemical hydrogen evolution – insights from first principles calculations, Phys. Chem. Chem. Phys. 17 (2015) 10823–10829, http://dx.doi.org/10.1039/C5CP01065A.
[23] H. Vogt, Electrosynthesis of chlorate in the nineteenth century, J. Electrochem. Soc. 128 (1981) 29C–32C.
[24] B. Endrodi, N. Simic, M. Wildlock, A. Cornell, A review of chromium(VI) use in chlorate electrolysis: functions, challenges and suggested alternatives, Electrochim. Acta 234 (2017) 108–122, http://dx.doi.org/10.1016/j.electacta.2017.02.150.
[25] K. Hedenstedt, N. Simic, M. Wildlock, E. Ahlberg, Current efficiency of individual electrodes in the sodium chlorate process: a pilot plant study, J. Appl. Electrochem. 47 (2017) 991–1008, http://dx.doi.org/10.1007/s10800-017-1100-3.
[26] K. Hedenstedt, N. Simic, M. Wildlock, E. Ahlberg, Kinetic study of the hydrogen evolution reaction in slightly alkaline electrolyte on mild steel, goethite and lepidocrocite, J. Electroanal. Chem. 783 (2016) 1–7.
[27] U. Schwertmann, U. Gasser, H. Sticher, Chromium-for-iron substitution in synthetic goethites, Geochim. Cosmochim. Acta 53 (1989) 1293–1297.
[28] H. Xu, T. Lou, Y. Li, Synthesis and characterize of trivalent chromium $Cr(OH)_3$ and Cr_2O_3 microspheres, Inorg. Chem. Commun. 7 (2004) 666–668.
[29] M. Aguilar, E. Barrera, M. Palomar-Pardavé, L. Huerta, S. Muhl, Characterization of black and white chromium electrodeposition films: surface and optical properties, J. Non-Cryst. Solids 329 (2003) 31–38.
[30] J.S. Sears, C.D. Sherrill, Assessing the performance of density functional theory for the electronic structure of metal-salens: The d2-metals, J. Phys. Chem. A 112 (2008) 6741–6752.
[31] J.S. Sears, C.D. Sherrill, The electronic structure of oxo-Mn(salen): Single-reference and multireference approaches, J. Chem. Phys. 124 (2006) 144314.
[32] C.J. Cramer, D.G. Truhlar, Density functional theory for transition metals and transition metal chemistry, Phys. Chem. Chem. Phys. 11 (2009) 10757–10816.
[33] S. Grimme, A. Hansen, A Practicable Real-Space Measure and Visualization of Static Electron-Correlation Effects, Angew. Chem. Int. Ed. 54 (2015) 12308–12313.
[34] B. Hammer, L.B. Hansen, J.K. Nørskov, Improved adsorption energetics within density-functional theory using revised Perdew-Burke-Ernzerhof functionals, Phys. Rev. B 59 (1999) 7413–7421.
[35] S.N. Steinmann, C. Corminbeouf, A generalized-gradient approximation exchange hole model for dispersion coefficients, J. Chem. Phys. 134 (2011) 044117.
[36] S.N. Steinmann, C. Corminbeouf, Comprehensive benchmarking of a density-dependent dispersion correction, J. Chem. Theory Comput. 7 (2011) 3567–3577.
[37] S.N. Steinmann, C. Corminbeouf, A system-dependent density-based dispersion correction, J. Chem. Theory Comput. 6 (2010) 1990–2001.
[38] P.E. Bloechel, Projector augmented-wave method, Phys. Rev. B 50 (1994) 17953–17979.
[39] M. Busch, E. Ahlberg, I. Panas, Validation of binuclear descriptor for mixed transition metal oxide supported electrocatalytic water oxidation, Catal. Today 202 (2013) 114–119, http://dx.doi.org/10.1016/j.cattod.2012.04.060.
[40] M. Busch, E. Ahlberg, I. Panas, Water oxidation on MnOx and IrOx: why similar performance? J. Phys. Chem. C 117 (2013) 288–292.
[41] M. Busch, E. Ahlberg, I. Panas, Electrocatalytic oxygen evolution from water on a Mn(III-V) dimer model catalyst - a DFT perspective, Phys. Chem. Chem. Phys. 13 (2011) 15069–15076.
[42] M. Busch, E. Ahlberg, I. Panas, Hydroxide oxidation and peroxide formation at embedded binuclear transition metal sites; TM = Cr, Mn, Fe, Co, Phys. Chem. Chem. Phys. 13 (2011) 15062–15068.
[43] M. Busch, N.B. Halck, U. Kramm, S. Siahrostami, P. Krtil, J. Rossmeisl, Beyond the top of the Volcano - A unified approach to electrocatalytic oxygen reduction and oxygen evolution, Nano Energy 29 (2016) 126–135, http://dx.doi.org/10.1016/j.nanoen.2016.04.011.
[44] R. Frydendal, M. Busch, N.B. Halck, E.A. Paoli, P. Krtil, I. Chorkendorff, J. Rossmeisl, Enhancing activity for the oxygen evolution reaction: the beneficial interaction of gold with manganese and cobalt oxides, ChemCatChem 7 (2015) 149–154, http://dx.doi.org/10.1002/cctc.201402756.
[45] J. Rossmeisl, Z.-W. Qu, H. Zhu, G.-J. Kroes, J.K. Nørskov, Electrolysis of water on oxide surfaces, J. Electroanal. Chem. 607 (2007) 83–99.
[46] I.C. Man, H.-Y. Su, F. Calle-Vallejo, H.A. Hansen, N.G. Martînez, J.I. Inoglu, J. Kitchin, T.F. Jaramillo, J.K. Nørskov, J. Rossmeisl, Universality in oxygen evolution electrocatalysis on oxide surfaces, ChemCatChem 3 (2011) 1159–1165, http://dx.doi.org/10.1002/cctc.201000397.
[47] K. Hedenstedt, J. Bäckström, E. Ahlberg, In-situ Raman spectroscopy of α- and γ-FeOOH during cathodic load, J. Electrochem. Soc. 164 (2017) H621–H627.
[48] H.D. Lutz, H. Möller, M. Schmidt, Lattice vibration spectra. Part LXXXII. Brucite-type hydroxides $M(OH)_2$ (M = Ca, Mn, Co, Fe, Cd) — IR and Raman spectra, neutron diffraction of $Fe(OH)_2$, J. Mol. Struct. 328 (1994) 121–132.
[49] M. Bajdich, M. García-Mota, A. Vojvodic, J.K. Nørskov, A.T. Bell, Theoretical investigation of the activity of cobalt oxides for the electrochemical oxidation of water, J. Am. Chem. Soc. 135 (2013) 13521–13530.
[50] H.-Y. Su, Y. Gorlin, I.C. Man, F. Calle-Vallejo, J.K. Nørskov, T.F. Jaramillo, J. Rossmeisl, Identifying active surface phases for metal oxide electrocatalysts: a study of manganese oxide bi-functional catalysts for oxygen reduction and water oxidation catalysis, Phys. Chem. Chem. Phys. 14 (2012) 14010–14022.
[51] M. Ortiz-Morales, J.J. Soto-Bernal, C. Frausto-Reyes, S.E. Acosta-Ortiz, R. Gonzalez-Mota, I. Rosales-Candelas, Raman spectroscopic analysis of iron chromium oxide microspheres generated by nanosecond pulsed laser irradiation on stainless steel, Spectrochim. Acta A 145 (2015) 505–510.
[52] S. Krehula, S. Musić, The influence of a Cr-dopant on the properties of α-FeOOH particles precipitated in highly alkaline media, J. Alloys Compd. 469 (2009) 336–342.
[53] J.E. Amonette, D. Rai, Identification of noncrystalline $(Fe,Cr)(OH)_3$ by infrared spectroscopy, Clay Clay Miner. 38 (1990) 129–136.
[54] S. Suzuki, Y. Takahashi, M. Saito, M. Kusakabe, T. Kamimura, H. Miyuki, Y. Waseda, Atomic-scale structure of α-FeOOH containing chromium by anomalous X-ray scattering coupled with reverse Monte Carlo simulation, Corros. Sci. 47 (2005) 1271–1284.
[55] S. Suzuki, Y. Takahashi, T. Kamimura, H. Miyuki, K. Shinoda, K. Tohji, Y. Waseda, Influence of chromium on the local structure and morphology of ferric oxyhydroxides, Corros. Sci. 46 (2004) 1751–1763.
[56] Y. Tang, F.M. Michel, L. Zhang, R. Harrington, J.B. Parise, R.J. Reeder, Structural properties of the Cr(III) − Fe(III) (Oxy)hydroxide compositional series: insights for a nanomaterial solid solution, Chem. Mater. 22 (2010) 3589–3598.
[57] A.E. Tufo, E.E. Sileo, P.J. Morando, Release of metals from synthetic Cr-goethites under acidic and reductive conditions: effect of aging and composition, Appl. Clay Sci. 58 (2012) 88–95.
[58] A.S.O. Gomes, N. Yaghini, A. Martinelli, E. Ahlberg, A micro-Raman spectroscopic study of $Cr(OH)_3$ and Cr_2O_3 nanoparticles obtained by the hydrothermal method, J. Raman Spectrosc. (2017), http://dx.doi.org/10.1002/jrs.5198.
[59] M. Stratmann, K. Hoffmann, In situ Mößbauer spectroscopic study of reactions within rust layers, Corros. Sci. 29 (1989) 1329–1352.
[60] M. Stratmann, K. Bohnekamp, H.-J. Engell, An electrochemical study of phase-transitions in rust layers, Corros. Sci. 23 (1983) 969–985.
[61] A. Kuch, Investigations of the reduction and re-oxidation kinetics of iron (III) oxide scales formed in waters, Corros. Sci. 28 (1988) 221–231.
[62] J. Dünnwald, A. Otto, An investigation of phase transition in rust layers using Raman spectroscopy, Corros. Sci. 29 (1989) 1167–1176.
[63] J. Monnier, S. Réguer, E. Foy, D. Testemale, F. Mirambet, M. Saheb, P. Dillmann, L. Guillot, XAS and XRD in situ characterisation of reduction and reoxidation processes of iron corrosion products involved in atmospheric corrosion, Corros. Sci. 78 (2014) 293–303.
[64] D.R. Wilburn, W.A. Bassett, Hydrostatic compression of iron and related compounds: an overview, Am. Mineral. 63 (1978) 591–596.
[65] D.A. Dzombak, F.M.M. Morel, Surface Complexation - Hydrous Ferric Oxides, Wiley, 1990.
[66] J. Rossmeisl, J.K. Nørskov, C.D. Taylor, M.J. Janik, M. Neurock, Calculated phase diagrams for the electrochemical oxidation and reduction of water over Pt(111), J.

Phys. Chem. B 110 (2005) 21833–21839.
[67] R.M. Cornell, U. Schwertmann, The Iron Oxides: Structure, Properties, Reactions, Wiley VCH, Weinheim, 1996.
[68] M. Busch, R.B. Wang, A. Hellman, J. Rossmeisl, H. Grönbeck, The Influence of Inert Ions on the Reactivity of Manganese Oxides, (Submitted) (n.d.).
[69] M. Lehtimäki, H. Hoffmannova, O. Boytsova, Z. Bastl, M. Busch, N.B. Halck, J. Rossmeisl, P. Krtil, Targeted design of α-MnO_2 based catalysts for oxygen reduction, Electrochim. Acta 191 (2016) 452–461.
[70] R.T. Shuey, Developments in Economic Geology - 4 Semiconducting Ore Minerals, Elsevier, Amsterdam, 1975.
[71] H. Asteman, E. Ahlberg, J.-E. Svensson, Electric properties of α-Fe_2O_3, Cr_2O_3 and α-$(Cr, Fe)_2O_3$ and their relevance to corrosion, Proc. - Electrochem. Soc. 99–38 (2000) 17–25.
[72] K. Hedenstedt, A.S.O. Gomes, M. Busch, E. Ahlberg, Study of Hypochlorite Reduction Related to the Sodium Chlorate Process, Electrocatalysis 7 (2016) 326–335, http://dx.doi.org/10.1007/s12678-016-0310-5.